Tuning topological superconductivity within the *t*-*J*-*U* model of twisted bilayer cuprates

Maciej Fidrysiak,* Bartłomiej Rzeszotarski, and Józef Spałek†
Institute of Theoretical Physics, Jagiellonian University, ul. Łojasiewicza 11, 30-348 Kraków, Poland

(Received 6 October 2023; revised 29 November 2023; accepted 30 November 2023; published 12 December 2023)

We carry out a theoretical study of unconventional superconductivity in twisted bilayer cuprates (TBCs) as a function of electron density and layer twist angle. The bilayer *t*-*J*-*U* model is employed and analyzed within the framework of a generalized variational wave function approach in the statistically consistent Gutzwiller formulation. The constructed phase diagram encompasses both a gapless d-wave state (reflecting the pairing symmetry of untwisted copper-oxides) and gapped $d + e^{i\varphi}d$ phase that breaks spontaneously time reversal symmetry (TRS) and is characterized by a nontrivial Chern number. We find that the $d + e^{i\varphi}d$ state occupies a nonconvex butterfly-shaped region in the doping versus twist-angle plane and demonstrate the presence of a reentrant TRS-breaking phase on the underdoped side of the phase diagram. This circumstance supports the emergence of topological superconductivity for fine-tuned twist angles in TBC away from 45°. Our analysis of the microscopically derived Landau free-energy functional points toward sensitivity of the superconducting order parameter to small perturbations close to the topological state boundary.

DOI: 10.1103/PhysRevB.108.224509

I. INTRODUCTION

Strong electronic correlations in condensed-matter materials are the driving force of a number of unique phenomena, among them high-temperature (SC), the pseudogap state, and non-Fermi liquid behavior. Unambiguous microscopic clarification of those and related effects is challenging and remains one of the major endeavors in condensed matter physics (cf. Ref. [1] for review). Successful execution of this task relies on the supply of diversified experimental data for a broad range of parameters and energy scales to provide the testing ground for contemporary theoretical models. A paradigm for an *ad hoc* engineering of highly tunable strongly correlated electron systems, offering such an insight, appeared following experimental realization of unconventional superconductivity and Mott insulating states in twisted bilayer graphene [2,3]. In this case, the interlayer twist-angle serves as the parameter providing control over electronic bandwidth, and thus allows us to drive the otherwise moderately correlated system into the strongly correlated regime. Analogous tunable strongly correlated states have also been reported for twisted transition metal dichalcogenides [4].

Recent progress in fabrication of high-temperature SC $Bi_2Sr_2CaCu_2O_{8+x}$ (Bi-2212) thin films [5,6] and monolayers, [7] with properties comparable to the bulk crystals, opens possibilities to explore physics of strong electronic correlations in two dimensions. Specifically, introducing a twist between the copper-oxide SC layers has been proposed to stabilize high-temperature $d + e^{i\varphi}d$ SC with nonzero phase φ between layer order parameters that spontaneously breaks time reversal symmetry (TRS) and hosts nontrivial topology [8]. This might be regarded as generalization of pure $d + id$ pairing and a concrete realization of the earlier proposals of TRS-breaking SC in Josephson junctions, composed of superconductors with distinct pairing symmetries (e.g., $d_{x^2-y^2}$ and d_{xy}) [9]. Subsequent theoretical studies of the Hubbard [10] and *t*-*J*-model [11] on twisted bilayer square lattice support this scenario, yet the resultant SC phase diagrams vary substantially, depending on the microscopic Hamiltonian and approximation employed, encompassing topological SC with large Chern numbers ($C = 2, 4, 8$) or a topologically trivial state ($C = 0$). An experimental search for possible formation of TRS-breaking SC in Bi-2212 [12–15] and $Bi_2Sr_{2-x}La_xCuO_{6+y}$ (Bi-2201) [16] provides ambiguous evidence regarding $d + id$ pairing and points toward the prevalence of an isotropic pairing component. Systematic characterization of the SC across the phase diagram of twisted bilayer cuprates (TBCs) is thus desired.

We carry out analysis of unconventional SC for TBCs in a broad range of twist angle and hole doping, from an underdoped to overdoped regime. A generalized *t*-*J*-*U* model on twisted square lattice is employed. This Hamiltonian incorporates both on-site Coulomb repulsion and antiferromagnetic exchange on equal footing, and has been previously utilized for a quantitative description of equilibrium and dynamic properties of untwisted materials [1]. The analysis is carried out within the framework of the statistically consistent Gutzwiller approximation (SGA), constituting a finite-temperature extension of the variational wave-function scheme that is applicable to large supercells, emerging in moiré systems. The obtained doping versus twist-angle phase diagram encompasses both plain gapless d-wave and topological TRS breaking $d + e^{i\varphi}d$ SC. Those states are separated by a series of quantum phase transitions concealed within the high-T_c SC dome inherited from the untwisted cuprates.

The $d + e^{i\varphi}d$ state is stabilized in a narrow layer twist angle regime around $\theta = 45°$, in agreement with former theoretical studies [8,10]. However, we reveal reentrant $d +$

*maciej.fidrysiak@uj.edu.pl
†jozef.spalek@uj.edu.pl

$e^{i\varphi}d$ SC emerging as a function of the layer twist angle in underdoped systems. Multiple characteristics of the SC state are analyzed throughout the high-T_c phase diagram, including the SC order parameter, equilibrium value of SC relative phase factor between the layers, and energy gap in the quasiparticle spectrum. In particular, we demonstrate that the onset of $d + e^{i\varphi}d$ SC is assisted by opening the energy gap, yet those two quantities follow distinct doping dependence; for certain values of the layer twist angle, we identify a double-dome-shaped gap as a function of electronic density (band filling). Finally, we extend our analysis of equilibrium SC properties and study the microscopically derived Landau free-energy functional, which encodes information about the stiffness of paired state. Close to the onset of TRS-breaking SC, free energy becomes extremely flat as a function of the relative SC phase factor between layers. This circumstance points toward sensitivity of the $d + e^{i\varphi}d$ order parameter to small perturbations, such as chemical disorder and interface imperfections, and might rationalize the ambiguous structure of the SC order parameter reported experimentally for twist angles close to $\sim 45^\circ$.

The paper is organized as follows. In Sec. II, we introduce the bilayer t-J-U model, and in Sec. III we discuss the symmetry of the SC order parameter and define relevant quantities. In Sec. IV, we present the results, encompassing SGA doping versus twist angle phase diagram, as well as the analysis of microscopically derived Landau free-energy landscape versus $d + e^{i\varphi}d$ pairing amplitude. A summary and discussion is given in Sec. V. Appendices A and B provide relevant details of our approach and multiple consistency checks of the employed methodology.

II. MODEL AND METHOD

For certain (commensurate) twist angles, the twisted bilayer square lattice forms a periodic superstructure. Those configurations are characterized by two integers, n and m, such that the layer twist angle reads $\theta = 2 \cdot \arctan(m/n)$. The number of copper atoms per unit cell reads then $N_{\text{cell}} = 2 \cdot (n^2 + m^2)$, with the factor of 2 reflecting the number of layers. The resultant superstructure forms a square with lattice spacing $a = \sqrt{n^2 + m^2}a_0$, where a_0 denotes the in-plane Cu-Cu distance. Hereafter, we set the total number of copper sites to $N_{\text{Cu}} \approx 80\,000$ which, as we verified, is sufficient to reliably represent the thermodynamic-limit situation. Note that it is not possible to form periodic lattices with exactly $N_{\text{Cu}} \equiv 80\,000$ sites for all considered twist angles, as the unit-cell dimensions are irrational numbers, in general. In Table I, we list the values of n and m addressed in the present paper, as well as lattice sizes and other relevant parameters. The unit cells of the resulting superstructures are illustrated in Figs. 1(a)–1(e), with the exception of the trivial case without a twist ($\theta = 0^\circ$) and those marked as *not included* in Table I. Blue and red circles represent Cu sites in layers A and B, respectively, and links visualize hybridization between layers. Copper sites in the left-bottom corner of the unit cell are positioned exactly on top of each other so the blue circle is not visible.

Remarkably, not all pairs of indices (n, m) result in new superstructures. Layers at twist angle θ may be transformed into those twisted by $\theta' = 90^\circ - \theta$ by appropriate spatial transformations and are thus physically equivalent in the thermodynamic limit. Small finite-size and boundary condition effects arising in finite geometries are discussed below. In effect, there is no need to explicitly consider lattices characterized by $n = 3, m = 1$ and $n = 5, m = 1$ as those are equivalent to $n = 2, m = 1$ and $n = 3, m = 2$ with smaller supercells (those are marked as *not included* in Table I; we use them only for test and benchmark purposes). The geometric construction illustrating this equivalence is displayed in Fig. 1(f). Blue and red coordinate axes correspond to the square lattices in layers A and B, respectively. The layers are rotated with respect to the original coordinate system $\hat{x}$-$\hat{y}$ (dotted arrows) by $+\theta/2$ (counter-clockwise) and $-\theta/2$ (clockwise), so the relative angle between layers reads θ. By carrying out a 45° counter-clockwise rotation around the out-of-plane $\hat{z}$ axis, followed by layer interchange, we effectively exchange the angles θ and $90^\circ - \theta$ marked in Fig. 1(f). In effect, with a limited number of superstructures, we are able to densely cover the range of twist angles $\theta \in [0, 90^\circ]$ and explore the structure of doping-θ phase diagrams for correlated lattice Hamiltonians on twisted square lattice.

We employ the t-J-U model [1,17], reformulated for the TBC system. It may be regarded as a formal generalization of Hubbard and t-J models, and encompasses both of them as particular cases. The Hubbard model is not well-suited for SGA and related (e.g., slave-boson) approximation schemes due to lack of explicit exchange interactions. The magnetic exchange processes emerge in subleading orders of respective diagrammatic expansions [18], making the problem intractable for large supercells addressed. In effect, low-order approximation solutions obtained within those three Hamiltonians may differ. The t-J and t-J-U models thus provide a methodological advantage over the complementary Hubbard-model description, allowing us to discuss the high-T_c SC already at the saddle-point-solution level. On the other hand, systematic variational wave function studies of both the t-J and t-J-U models demonstrate that the t-J-U model

TABLE I. Characteristics of the twisted square-lattice bilayer for selected twist angles, θ. Commensurate configurations are determined by two integers, n and m, such that $\theta = 2 \cdot \arctan(m/n)$. N_{cell} is the number of atoms in the unit cell, and N_{Cu} denotes the total number of Cu sites in the lattice (periodic boundary conditions are imposed and lattice dimensions have been selected so N_{Cu} is close to 80 000). Superstructure lattice constant is also given, in the units of the Cu-Cu distance a_0. Inequivalent lattices used in the present paper are marked in the last column as *included*. Those *not included* are related by symmetry to other superlattices with smaller unit cells, as discussed in the text.

n	m	N_{cell}	N_{Cu}	a/a_0	θ (°)	$90^\circ - \theta$ (°)	Included
1	0	2	80 000	1.000	0.00	90.00	yes
2	1	10	79 210	2.236	53.13	36.87	yes
3	1	20	79 380	3.162	36.87	53.13	no
3	2	26	78 650	3.606	67.38	22.62	yes
4	1	34	78 336	4.123	28.07	61.93	yes
4	3	50	80 000	5.000	73.74	16.26	yes
5	1	52	79 092	5.099	22.62	67.38	no
5	2	58	79 402	5.385	43.60	46.40	yes

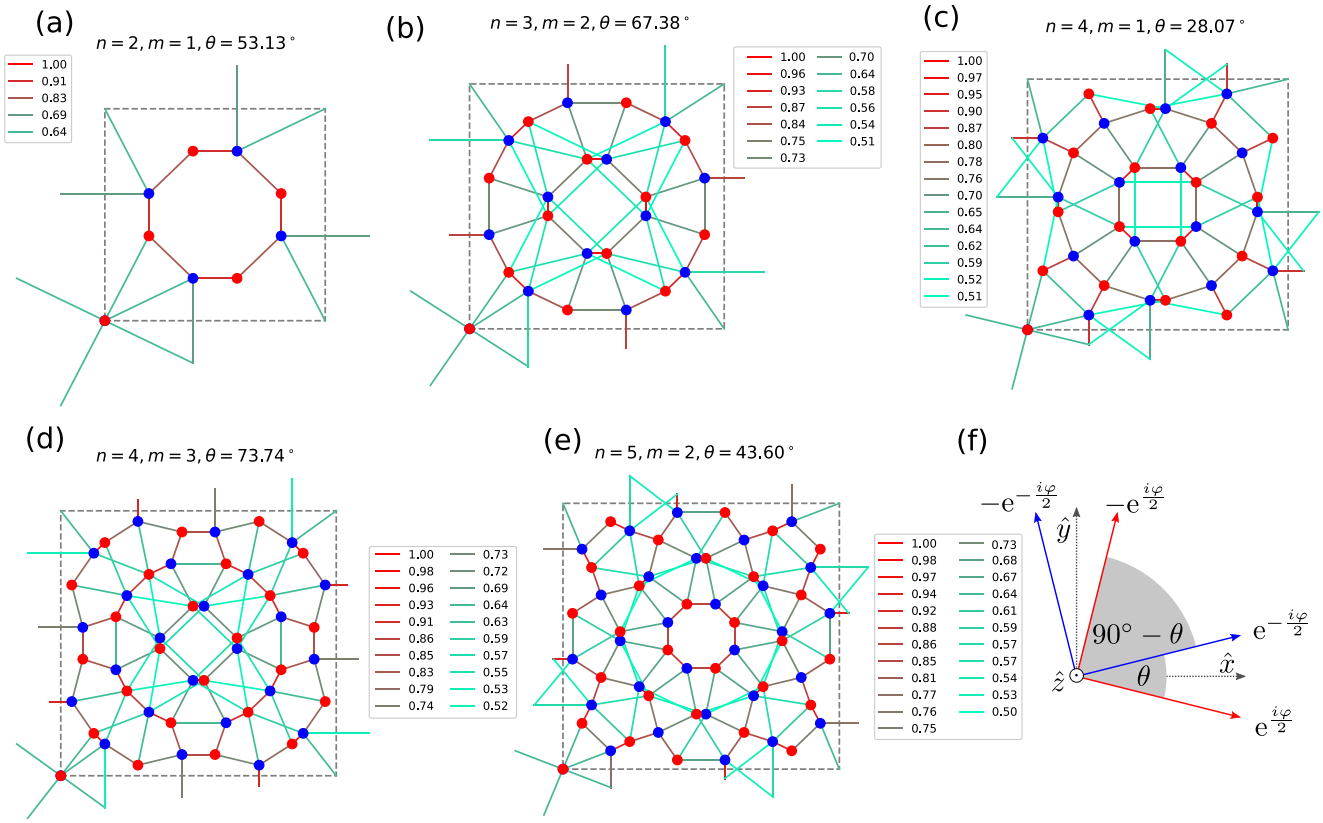

FIG. 1. Top view of the unit cell for twisted-bilayer square lattice. Blue and red circles are copper sites in the lower- and upper-layers, respectively, and links represent interlayer hybridization, V_{ij}, here given in the units of V_0 [cf. Eq. (3)]. Only links corresponding to hybridization $V_{ij} \geqslant 0.5V_0$ are marked for clarity (magnitudes of V_{ij}/V_0 are detailed in the legend). Note that the copper sites in neighboring layers in the left-bottom corner of the unit cell are positioned exactly on top of each other, and blue circle is not visible. (a)–(e) correspond to twist angles $\theta = 53.13^\circ$, 67.38°, 28.07°, 73.74°, and 43.60°, respectively. (f) illustrates the symmetry of $d + e^{i\varphi}d$ superconducting order parameter in twisted square lattice. Blue and red coordinate axes correspond to the layers, twisted by and angle $\pm\theta/2$ with respect to the original coordinate frame (dotted axes). Phases of the layer order parameters $\pm\exp(\pm i\varphi/2)$ along the directions parallel to the axes are also marked, as explained in the text. As follows from (f), system at twist angle θ may be transformed into that twisted by complementary $\theta' = 90^\circ - \theta$ by means of a 45° lattice rotation along the out-of-plane $\hat{z}$ direction, combined with the interchange of A and B planes. The data for complementary angles $\theta' = 36.87^\circ$, 61.93°, 16.26°, and 46.40° are thus obtained by transforming those for supercells (a)–(e), and there is no need to consider them explicitly.

yields a better global description of high-T_c cuprates across their phase diagram than the t-J model [1]. In particular, the t-J-U model reproduces quantitatively experimental doping dependence of the effective masses and Fermi velocity [1], as well as correctly accounting for certain subtle SC properties, including a crossover between BCS-like to non-BCS-like regimes. The latter effect occurs at the single meV scale and is characterized by the sign change of kinetic energy gain at the SC transition [17,19,20]. Since the free-energy landscape for TBC involves even smaller energy scales, we consider the t-J-U model as an appropriate departure point for addressing unconventional SC in those systems.

An attractive methodological feature of the t-J-U Hamiltonian is that calculations in restricted (projected) Hilbert space, with doubly occupied sites excluded, are not necessary. This is because the large value of on-site Coulomb repulsion to hopping ratio $\sim$20 essentially reduces the value of doubly occupancy probability, d^2. Typically, $d^2 \lesssim 10^{-2}$, which is much smaller than the weak-coupling-limit value $d^2 \sim 0.2$. Hence, the considered model reflects the principal features of t-J model physics. Moreover, the presence of the exchange term $\propto J$ also accounts for additional superexchange channels beyond the Anderson kinetic exchange, which is of too small a magnitude for the realistic values of hopping and Coulomb interaction taken for the cuprates. Nevertheless, even in the present strong-correlation regime ($U/|t| \sim 20$) and nonzero doping, the double occupancy probability is small but nonzero. The limit of the t-J model is thus approached, but not formally reached [21]. This and other aspects of the approach have been elaborated on at length in our previous papers [1,1].

For each of the two layers, $L = A, B$, the respective t-J-U Hamiltonians read

$$\hat{\mathcal{H}}^{(L)}_{t\text{-}J\text{-}U} = \sum_{\substack{\langle i,j\rangle \\ i,j\in L}} (t_{ij}\hat{a}^\dagger_{i\sigma}\hat{a}_{j\sigma} + \text{H.c.}) + \sum_{\substack{\langle i,j\rangle \\ i,j\in L}} J_{ij}\hat{\mathbf{S}}_i\hat{\mathbf{S}}_j + U\sum_{i\in L}\hat{n}_{i\downarrow}\hat{n}_{i\uparrow}, \tag{1}$$

where $\hat{a}_{i\sigma}$ ($\hat{a}^\dagger_{i\sigma}$) annihilate (create) electrons on lattice site i (note that the operators are not projected as in the t-J model

TABLE II. Summary of the bilayer t-J-U-model parameters employed in the present paper. Except for the value on nearest-neighbor hopping, t, the energies are expressed in the units o $|t|$. The interlayer distance and tunneling decay length [cf. Eq. (3)] are expressed in terms of in-plane Cu-Cu distance, a_0. The analysis has been carried out for two values of $J/|t| = 0.3$ and 0.4.

Parameter	Value	Description
t	-0.35 eV	nearest-neighbor hopping
$t'/\|t\|$	0.3	next-nearest-neighbor hopping
$U/\|t\|$	20	on-site Coulomb repulsion
$J/\|t\|$	0.3, 0.4	exchange interaction
$V_0/\|t\|$	-0.2	interlayer tunneling magnitude
d/a_0	2.1	interlayer distance
r_0/a_0	0.5	tunneling decay length
$k_BT/\|t\|$	10^{-6}	temperature

[21]). In Eq. (1), $\langle i, j\rangle$ means that each pair of indices appears only once in the summation, whereas t_{ij} and J_{ij} denote hopping and exchange integrals, respectively. The Hubbard- and t-J-model limits are retrieved for $J = 0, U \neq 0$ and $J \neq 0, U \to \infty$, as discussed above. Hereafter, we retain only hopping integrals between nearest and next-nearest neighbors, $t = -0.35$ eV and $t' = 0.3|t|$, and the on-site Coulomb repulsion is set to $U = 20|t|$. This means that the ratio U/W is large, but not yet in the canonical t-J-model limit. We consider two values of the antiferromagnetic nearest-neighbor exchange, $J = 0.3|t|$ and $0.4|t|$, to assess how the intralayer pairing affects the interlayer SC correlations. Moreover, in our calculations, we retain small finite temperature $T = 10^{-6}|t|/k_B$, where k_B denotes Boltzmann constant. Microscopic parameters in this range have been previously employed to study high-T_c SC [17] and interlayer tunneling effects [22] in untwisted ($\theta = 0^\circ$) systems.

The layers, A and B, are subsequently twisted by an angle $\theta \in [0^\circ, 90^\circ]$, as illustrated in Fig. 1, and coupled by interlayer tunneling V_{ij} so the total system Hamiltonian takes the form

$$\hat{\mathcal{H}} = \hat{\mathcal{H}}^{(A)}_{t\text{-}J\text{-}U} + \hat{\mathcal{H}}^{(B)}_{t\text{-}J\text{-}U} + \sum_{\substack{i\in B\\ j\in A,\sigma}} (V_{ij}\hat{a}^\dagger_{i\sigma}\hat{a}_{j\sigma} + \text{H.c.}), \tag{2}$$

whereas V_{ij} generally contains both isotropic and anisotropic components [11,23], here we restrict to a model situation with pure isotropic and exponentially decaying tunneling

$$V_{ij} = V_0 e^{-\frac{||\mathbf{r}_i - \mathbf{r}_j|| - d}{r_0}}, \tag{3}$$

where $\mathbf{r}_i$ denotes the position of lattice-site i, d is interlayer distance, and r_0 represents the characteristic decay length of the interaction between layers. Equation (3) is written so $V_{ij} \equiv V_0$ whenever site i is positioned directly on top of site j. In effect, V_0 becomes a direct measure of the overall interlayer hopping magnitude. Hereafter, for all calculations we use $V_0 = -0.2|t|$, $d = 2.1a_0$, $r_0 = 0.5a_0$, with a_0 being the interlayer Cu-Cu distance. Moreover, to make the problem tractable, we apply a cutoff to interlayer hybridization by discarding all V_{ij} such that $||\mathbf{r}_i - \mathbf{r}_j|| > 3.1a_0$. The model parameters employed in the present paper are summarized in Table II.

The model is analyzed within the framework of the variational wave-function approach in the SGA formulation. In its plain form, the varietal method is based on optimization of the energy functional

$$E_{\text{var}} \equiv \frac{\langle\Psi_{\text{var}}|\hat{\mathcal{H}}|\Psi_{\text{var}}\rangle}{\langle\Psi_{\text{var}}|\Psi_{\text{var}}\rangle}, \tag{4}$$

where $|\Psi_{\text{var}}\rangle$ is a variational state accounting for strong electronic correlations on copper sites. SGA provides an extension of the latter to finite temperature and introduces simplifications that makes the study of large lattices and supercells feasible. The methodological details are presented in Appendix A.

III. SUPERCONDUCTIVITY AND ORDER PARAMETER

Untwisted high-T_c copper-oxides host $d_{x^2-y^2}$ SC that is compatible with square-lattice symmetry and allows the electrons forming Cooper pairs to effectively avoid strong on-site Coulomb interactions. The constituents comprising natural building blocks for the SC order parameter of twisted bilayer are thus two intralayer $d_{x^2-y^2}$-wave order parameters $\Delta_d^{(A)} \equiv \langle\hat{\Delta}_d^{(A)}\rangle$ and $\Delta_d^{(B)} \equiv \langle\hat{\Delta}_d^{(B)}\rangle$, with their respective pairing operators

$$\hat{\Delta}_d^{(A)} = \frac{1}{4N_{\text{Cu}}}\sum_{i\in A}(\hat{a}_{i+\hat{x}_A\downarrow}\hat{a}_{i\uparrow} - \hat{a}_{i+\hat{x}_A\uparrow}\hat{a}_{i\downarrow} - \hat{a}_{i\hat{y}_A\downarrow}\hat{a}_{i\uparrow} + \hat{a}_{i+\hat{y}_A\uparrow}\hat{a}_{i\downarrow}) \tag{5}$$

and

$$\hat{\Delta}_d^{(B)} = \frac{1}{4N_{\text{Cu}}}\sum_{i\in B}(\hat{a}_{i+\hat{x}_B\downarrow}\hat{a}_{i\uparrow} - \hat{a}_{i+\hat{x}_B\uparrow}\hat{a}_{i\downarrow} - \hat{a}_{i+\hat{y}_B\downarrow}\hat{a}_{i\uparrow} + \hat{a}_{i+\hat{y}_B\uparrow}\hat{a}_{i\downarrow}). \tag{6}$$

In Eqs. (5) and (6), $\hat{x}_A = (\cos\frac{\theta}{2}, \sin\frac{\theta}{2}, 0)$, $\hat{y}_A = (-\sin\frac{\theta}{2}, \cos\frac{\theta}{2}, 0)$, $\hat{x}_B = (\cos\frac{\theta}{2}, -\sin\frac{\theta}{2}, 0)$, $\hat{y}_B = (\sin\frac{\theta}{2}, \cos\frac{\theta}{2}, 0)$ are the basis vectors for sublattices A and B, here expressed in the units of the Cu-Cu in-plane distance. The above expressions are normalized by N_{Cu} and an additional factor of 4 to take into account four expectation values appearing in the summation. We have found that, for twisted lattice structures displayed in Figs. 1(a)–1(e), the initially imposed d-wave intralayer symmetry is preserved throughout SGA self-consistent procedure; no admixture of extended s-wave components,

$$\hat{\Delta}_s^{(A)} = \frac{1}{4N_{\text{Cu}}}\sum_{i\in A}(\hat{a}_{i+\hat{x}_A\downarrow}\hat{a}_{i\uparrow} + \hat{a}_{i+\hat{x}_A\uparrow}\hat{a}_{i\downarrow} + \hat{a}_{i\hat{y}_A\downarrow}\hat{a}_{i\uparrow} + \hat{a}_{i+\hat{y}_A\uparrow}\hat{a}_{i\downarrow}), \tag{7}$$

$$\hat{\Delta}_s^{(B)} = \frac{1}{4N_{\text{Cu}}}\sum_{i\in B}(\hat{a}_{i+\hat{x}_B\downarrow}\hat{a}_{i\uparrow} + \hat{a}_{i+\hat{x}_B\uparrow}\hat{a}_{i\downarrow} + \hat{a}_{i+\hat{y}_B\downarrow}\hat{a}_{i\uparrow} + \hat{a}_{i+\hat{y}_B\uparrow}\hat{a}_{i\downarrow}), \tag{8}$$

is observed, even for largest considered supercells.

The layer order parameters $\Delta_d^{(A)}$ and $\Delta_d^{(B)}$ are generally complex numbers. Since the Hamiltonians for the two layers are equivalent [cf. Eq. (1)] and the hybridization V_{ij} acts symmetrically on A and B layers, the order parameter

amplitudes may be considered equal $|\Delta_d^{(A)}| = |\Delta_d^{(B)}|$, which we have also verified numerically. In turn, the single parameter $\Delta_{SC} \equiv |\Delta_d^{(A)}| = |\Delta_d^{(B)}|$ is hereafter used as a dimensionless measure of superconducting correlations. Moreover, the self-consistently obtained relative phase $\varphi \equiv \arg(\Delta_d^{(B)}/\Delta_d^{(A)})$ turns out generally nontrivial, constituting a physically sound quantity. The equilibrium value of φ different from 0° and 180° (modulo 360°) implies spontaneous breakdown of TRS, and admits nontrivial topology of the SC state. This is caused by the circumstance that under time-reversal operation, the phase is transformed as $\varphi \to -\varphi$, leading to ground-state degeneracy. With the help of global $U(1)$ gauge transformation, layer order parameters may be generically brought to the form $\Delta_d^{(A)} = |\Delta_d^{(A)}| \exp(-i\varphi/2)$ and $\Delta_d^{(B)} = |\Delta_d^{(B)}| \exp(i\varphi/2)$. The directional dependence of the order-parameter phase is marked in Fig. 1(f) next to the respective coordinate axes. Within each of the layers, the phase factor changes signs following spatial rotation by 90°. The relative phase between A- and B-layer order parameters is fixed at φ, which correspond to the $d + e^{i\varphi}d$ SC.

The above considerations let us relate the order parameters between the superstructures for complementary twist angles (θ and $\theta' \equiv 90^\circ - \theta$), cf. Table I. For the system at the twist angle θ whose free energy has degenerate minima at $\pm\varphi$, one can carry out the transformation to the θ' case following the procedure described in Sec. II. As follows from Fig. 1(f), the phase angles $\pm\varphi$ are then transformed into $180^\circ \pm \varphi$. This circumstance substantially reduces the computational cost of evaluating phase diagrams and is utilized below.

IV. RESULTS

A. Identification of gapped and gapless states

Before detailed presentation of the obtained phase diagrams, in Fig. 2 we characterize the relevant aspects of SC for two complementary twist angles, $\theta = 53.13^\circ$ (blue symbols) and $\theta = 36.87^\circ = 90^\circ - 53.13^\circ$ (red symbols), cf. Table I. The calculations have been carried out for the t-J-U model Eq. (2) with $J = 0.4|t|$ (left panels) and $J = 0.3|t|$ (right panels). The remaining model parameters are given in Sec. II. From top to bottom, the panels detail electron-density dependence of the SC order parameter Δ_{SC} [Figs. 2(a) and 2(d)], equilibrium SC relative phase φ [Figs. 2(b) and 2(e)], and the energy gap defined as the minimum energy for creating a particle-hole excitation [Figs. 2(c) and 2(f)]. For either selection of J, the order parameter [Figs. 2(a) and 2(d)] takes a typical domelike shape with a maximum close to 20% hole doping. Remarkably, the SC phase angle φ [Figs. 2(b) and 2(e)] also forms a dome along the electron-density axis, yet it encompasses only a fraction of the SC phase diagram. The nontrivial value of $\varphi \neq 0^\circ, 180^\circ$ (modulo 360°) indicates spontaneous TRS breakdown and emergence of topological SC. The latter is characterized by a nonzero gap in the energy spectrum [cf. Figs. 2(c) and 2(f)] and Chern number $C = 4$. To obtain perfectly quantized Chern numbers, we employ an efficient Brillouin-zone triangulation scheme [24] that yields essentially roundoff-error limited results. Such accuracy is needed to unambiguously characterize the weak SC state topology close to the $d + e^{i\varphi}d$ dome boundary, as evidenced

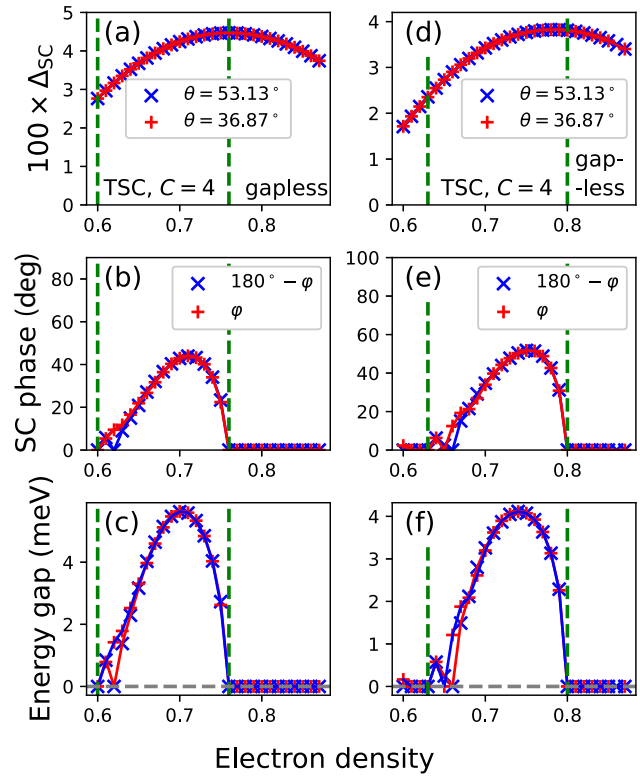

FIG. 2. Electron-density (doping) dependence of the calculated order parameter equilibrium value [(a), (d)], relative SC phase between layers, φ [(b), (e)], and energy gap in the quasiparticle spectrum [(c), (f)] for two complementary twist angles $\theta = 53.13^\circ$ (blue symbols) and $\theta = 36.87^\circ = 90^\circ - 53.13^\circ$ (red symbols). Those two selections of θ correspond to different unit cells ($n = 2, m = 1$ and $n = 3, m = 1$, respectively, cf. Table I), but are related by symmetry. Quantitative agreement of the two independent simulation results validates our supercell Hamiltonians and approach. (a)–(c) and (d)–(f) correspond to antiferromagnetic exchange $J = 0.4|t|$ and $J = 0.3|t|$, respectively. The remaining model parameters are detailed in the text. Vertical green dashed lines mark the quantum phase transitions between gapless d-wave and gapped topological SC (TSC) states. The TSC state is characterized by nontrivial Chern number $C = 4$.

by fractional numerical values of Chern numbers reported within other schemes [11]. On the other hand, for $\varphi = 0^\circ$ or 180°, the SC state is gapless due to the nodal structure inherited from the layer d-wave order parameters. In effect, there are two hidden quantum phase transitions within the SC dome, separating gapless and gapped topological SC (TSC) states. One is located close to optimal doping and the other appears in the overdoped regime; both are marked by dashed vertical lines.

Figure 2 also provides a stringent test of our theoretical framework. The displayed phase diagrams for complementary angles $\theta = 53.13^\circ$ and $\theta = 36.87^\circ = 90^\circ - 53.13^\circ$ have been obtained by independent simulations carried out for different supercells ($n = 2, m = 1$ and $n = 3, m = 1$, cf. Table I). The collapse of the order parameter and energy gaps indicates physical equivalence of those configurations, as predicted on symmetry grounds. Moreover, the self-consistently obtained equilibrium values of φ for those twist angles are compatible

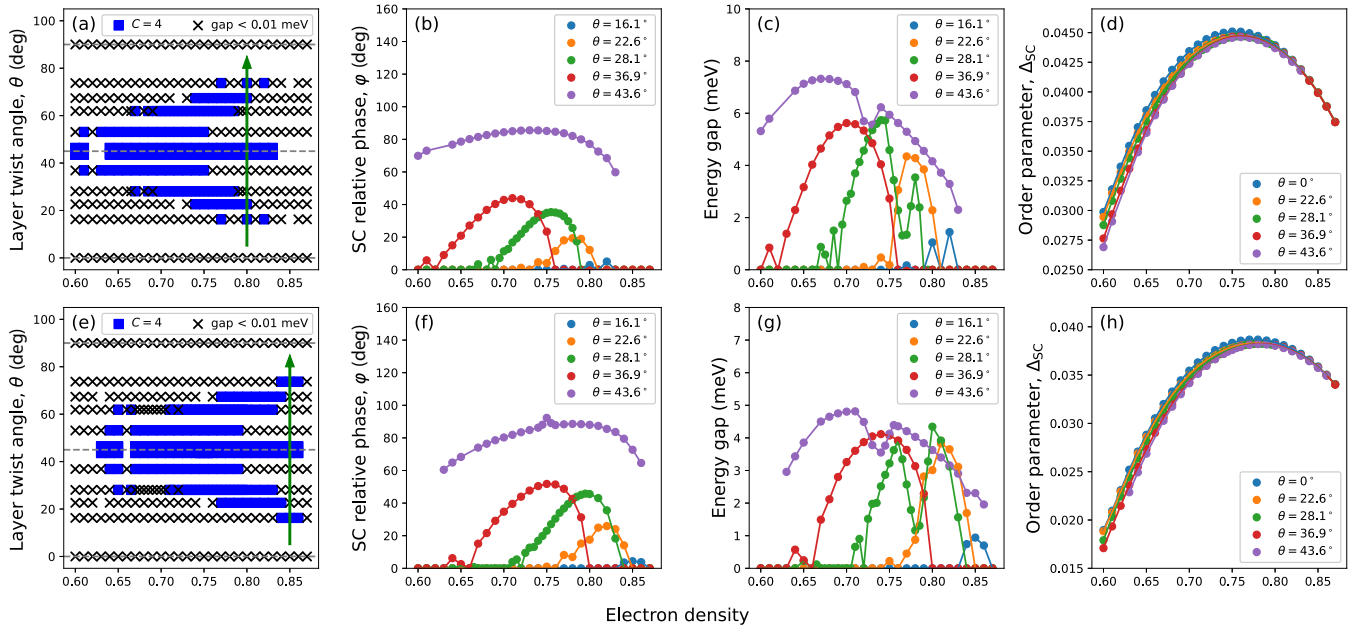

FIG. 3. Summary of variational wave-function results for twisted square-lattice bilayer t-J-U model for $J = 0.4|t|$ (top panels) and $J = 0.3|t|$ (bottom panels). The remaining model parameters are detailed in the main text. (a), (e) The obtained doping versus twist-angle phase diagrams, with gapless d-wave state marked by black crosses (numerically, gap $< 10^{-2}$ eV), and gaped topological SC (Chern number $C = 4$). For both values of antiferromagnetic exchange, butterfly-shaped gapped phase is obtained, indicating reentrant TRS-breaking $d + e^{i\varphi}d$ SC on the underdoped side of the phase diagram. Exemplary constant-density lines, for which reentrant $d + e^{i\varphi}d$ SC is observed, are marked by green arrows in (a) and (e). The remaining panels show doping dependence of relative SC phase between layers φ [(b), (f)], energy gap in the quasiparticle spectrum [(c), (g)], and intraplane SC order parameter Δ_{SC} [(d), (h)].

with the transformation rules introduced above [cf. Figs. 2(b) and 2(e)]; the free energy minima at $\pm\varphi$ for twist angle θ transforms into $180^\circ \pm \varphi$ at complementary angle $90^\circ - \theta$. Small quantitative differences observed at the boundaries of SC domes originate from finite-size and boundary-condition effects, as explained in Appendix B.

B. Doping versus twist angle phase diagrams

We now generalize the results of Fig. 2 and present the complete doping versus twist-angle phase diagrams in Fig. 3. Top and bottom panels correspond to antiferromagnetic exchange $J = 0.4|t|$ and $0.3|t|$, respectively, with other parameters remaining the same as those listed in Sec. II. Black symbols in Figs. 2(a) and 2(e) mark the gapless SC state (numerically, gap below 10^{-2} meV is regarded as zero) and blue crosses represent gapped topological $d + e^{i\varphi}d$ state with Chern number $C = 4$. Missing symbols for some combinations of θ and density indicate that we were unable to reach the absolute precision of 10^{-10} for the correlation functions, required to reliably determine order-parameter relative phase, φ (cf. the discussion of the computational aspects in Appendix B). The most distinctive feature of the phase diagrams, displayed in Figs. 2(a) and 2(e), is the nonconvex butterfly-shaped region of the TRS-breaking $d + e^{i\varphi}d$ state for both considered values of J. The nonconvexity manifests itself as a reentrant behavior of topological SC as a function of bilayer twist angle above optimal doping. Green arrows in Figs. 2(a) and 2(e) mark exemplary constant-density paths inside the phase diagram along which reentrance is observed. Whereas realization of topological SC in the $\theta \sim 45^\circ$ region is obstructed by detailed angular structure of interlayer tunneling [11,23], the $d + e^{i\varphi}d$ state might emerge for twist angles in the reentrant-SC range $\theta \sim$ 20-30° sufficiently close to half filling.

The remaining part of Fig. 3 details the doping dependence of relevant SC-state characteristics across the phase diagram. Figures 3(b) and 3(f) show the equilibrium SC phase angle between layers, φ. The range of densities, for which nontrivial φ is obtained, shrinks and shifts toward half filling with decreasing θ. Figures 3(c) and 3(g) detail the corresponding gaps in the quasiparticle spectrum, varying in the range 0–8 meV. The gapped state overlaps with the regime of TRS breaking $d + e^{i\varphi}d$ SC. Interestingly though, the relation between energy gaps and φ is not straightforward as those two quantities exhibit a qualitatively different doping dependence for specific combination of microscopic parameters. This is clearly seen for $\theta = 28.1^\circ$ and $J = 0.3|t|$ [green symbols in Figs. 3(f) and 3(g)]. Whereas φ forms a single dome as function of electron density, the corresponding energy gap splits into two overlapping domes centered at $n \approx 0.75$ and $n \approx 0.80$. To a lesser degree, such a dip in energy gap is also observed at $\theta = 43.6^\circ$. With the use of finite-size scaling, we have verified that the dip in the energy gap for $\theta = 28.1^\circ$ is not a numerical artifact and thus is of physical significance. Indeed, in Fig. 4 we compare the doping dependence of SC characteristics for $\theta = 28.1^\circ$ and two lattice sizes, $N_{Cu} = 78\,336$ (blue symbols) and $N_{Cu} = 319\,906$ (red symbols). All relevant quantities: Order parameter Δ_{SC} (a), phase angle φ (b), and energy gaps (c) overlap for different values of N_{Cu}. In particular, two-dome structure is robust against finite-size scaling, supporting our conclusion. Finally, Figs. 3(d) and 3(h) of the phase diagram

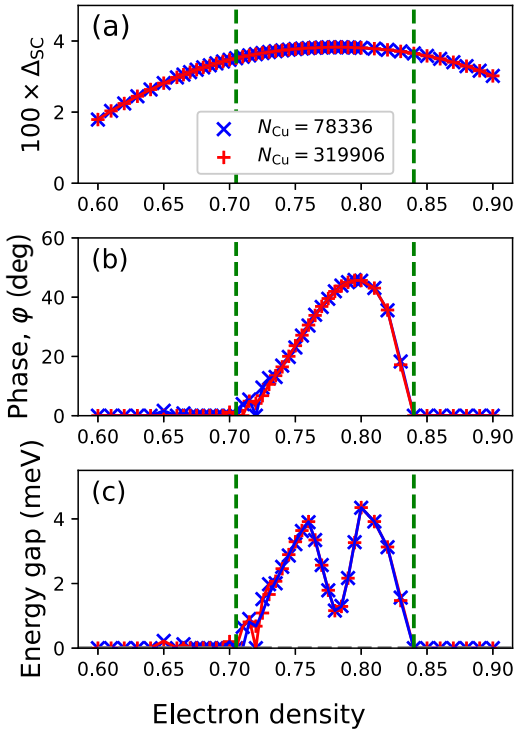

FIG. 4. Electronic-density dependence of the principal SC state characteristics, obtained for $J = 0.3|t|$ and layer twist angle $\theta = 28.07°$. The remaining microscopic model parameters are the same as those used to generate phase diagrams of Fig. 3. Blue and red curves correspond to the total number of Cu sites $N_{Cu} = 78\,336$ and 319 906, respectively. Vertical dashed lines mark quantum phase transitions between gapped and gapless states inside the SC dome. All the displayed quantities qualitatively agree for different lattice sizes, i.e., SC order parameter Δ_{SC} (a), relative SC phase φ (b), and energy gap (c). In particular, the two-dome structure of energy gap in (c) is robust against finite-size scaling, indicating that it is not a numerical artifact.

detail the interlayer d-wave order parameter, Δ_{SC}, forming a typical superconducting dome. Variation of the twist angle only weakly affects the magnitude of SC correlations within the layers, as those are mostly inherited form the untwisted materials. From the comparison of panels (d) and (h) with panels (a) and (e) of Fig. 3, it becomes apparent that the boundary of reentrant topological SC is positioned close to optimal doping.

C. Landau free-energy functional and robustness of topological superconductivity

We now address the hierarchy of energy scales related to SC transition in twisted bilayers, which goes beyond the equilibrium analysis summarized in Figs. 2 and 3. For the parent (untwisted) system, the relevant quantity is condensation energy, ΔF_{SC}, defined as the difference between the normal- and paired-state free energies per Cu site, $\Delta F_{SC} \equiv F_N - F_{SC}$. It should be emphasized that there is a degree of arbitrariness to the theoretical treatment of ΔF_{SC} for a high-temperature superconductor as the normal-state free energy, F_N, may be identified with either the pseudogap phase or

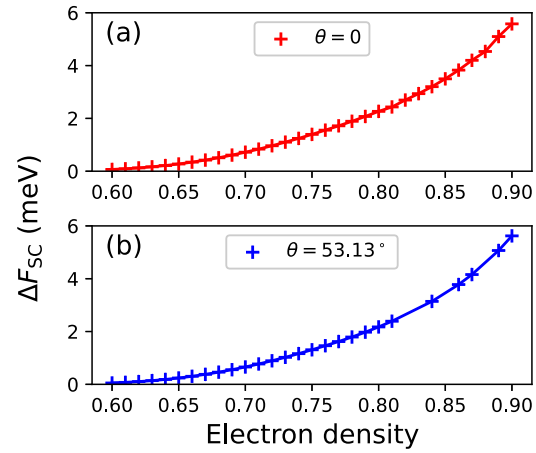

FIG. 5. Condensation energy ΔF_{SC} for bilayer t-J-U model as a function of electron density per copper site for (a) $\theta = 0°$ and (b) $\theta = 53.13°$. Antiferromagnetic exchange is set to $J = 0.3|t|$ and the remaining parameters are provided in the main text. The magnitude of ΔF_{SC} varies in single meV range.

correlated Fermi liquid. Here we adopt that latter convention and assume that F_N corresponds to the renormalized Fermi liquid, since a pure pseudogap without coexistent SC is not easily described within the present variational scheme. Those aspects, as well as a possible relation between pseudogap and SC, have been addressed previously in the context of gossamer SC within a Gutzwiller-type approach [25]. In effect, the thus defined ΔF_{SC} combines contributions attributed to both SC and pseudogap states on the underdoped side of the phase diagram. A monotonic increase of ΔF_{SC} is therefore expected as half filling is approached, in contrast to the domelike behavior reported based on thermodynamic measurements [26,27]. In Fig. 5, we display calculated ΔF_{SC} as a function of electronic density per Cu atom for two selected layer twist angles, $\theta = 0°$ and $\theta = 53.13°$. In either case, ΔF_{SC} varies within the meV range. Remarkably, $\Delta F_{SC} \lesssim 1$ meV in the overdoped regime, where no pseudogap contribution is present. This is somewhat larger, but within the same order of magnitude as estimates from specific heat measurements for Bi2212 [20,26].

In the case of bilayer, the free energy in the SC state may be regarded as a function of an additional parameter, i.e., relative phase φ. Variation of the Landau free energy $F(\varphi)$ for $\varphi \in [0, 360°]$ defines the second energy scale $\Delta F'_{SC}$. Below, we demonstrate that those two scales obey strict hierarchy $\Delta F'_{SC} \ll \Delta F_{SC}$. This renders topological SC fragile against small perturbations (e.g., those induced by disorder) and makes realization of the homogeneous $d + e^{i\varphi}d$ state challenging. A methodological remark is in order at this point. Strictly speaking, the thermodynamic system free energy F is not a functional of either Δ_{SC} or φ. To determine $\Delta F'_{SC}$, one thus needs to evaluate the Landau free-energy functional $F(\varphi)$ as a Legendre transform of the generalized free energy $F(\mathbf{J})$ in the presence of background currents $\mathbf{J}$ coupled linearly to the bilayer $d + e^{i\varphi}d$ order parameter. This procedure is detailed in Appendix B.

In Fig. 6, we plot the Landau free-energy functional, $F(\varphi)$, for fixed $\theta = 53.13°$ and various selections of electron density

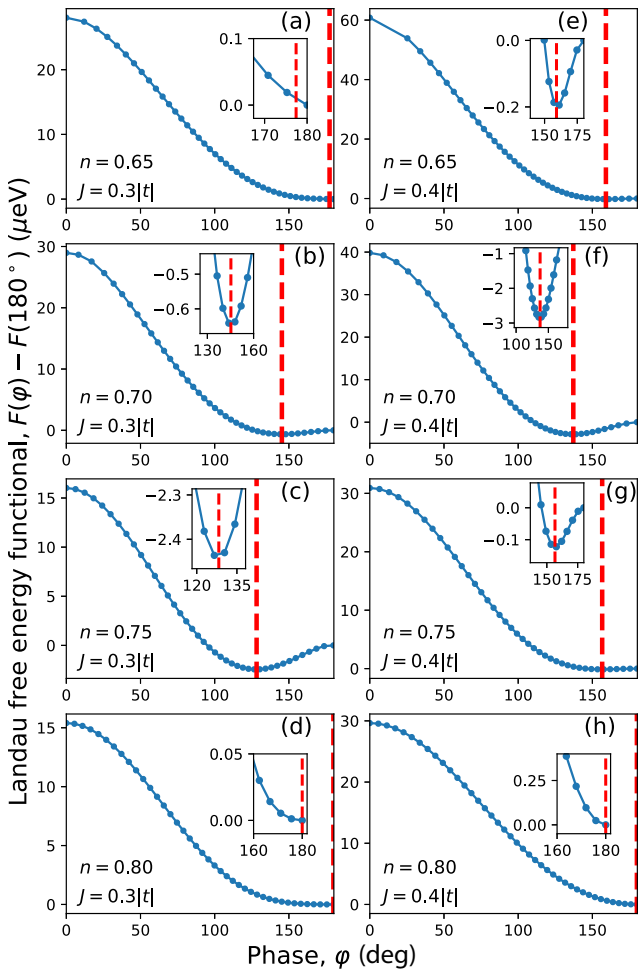

FIG. 6. Landau free-energy functional, $F(\varphi)$, as a function of relative phase SC between, φ. The layer twist angle is set to $\theta = 53.13^\circ$, and values of antiferromagnetic exchange J and electron density n are detailed inside the panels. The remaining parameters are given in the main text. Blue points represent $F(\varphi)$ evaluated for background field magnitude $J_0 = 0.003|t|$ (cf. Appendix B for details). Dashed red vertical lines represent the exact equilibrium values of phase φ, obtained by self-consistent SGA calculation. Insets detail $F(\varphi)$ close to the minima, and demonstrate that the SGA value of φ indeed corresponds to its minimum. Note that the Landau free-energy functional varies at the μeV scale and thus requires a careful numerical analysis to achieve reliable results.

and exchange coupling J, covering the phase diagrams displayed in Fig. 3. Left and right panels correspond to $J = 0.3|t|$ and $0.4|t|$, respectively. The unspecified model parameters are the same as those given in Sec. II. Points are obtained from SGA calculation and lines are guides to the eye. Insets inside the panels show the close-up view of $F(\varphi)$ close to minimum, and dashed vertical lines mark the value of φ obtained by self-consistent calculation without external currents (and thus representing the true equilibrium solution).

We note that the minimum of $F(\varphi)$ coincides with the self-consistently obtained value of SC relative phase, φ. This demonstrates that $F(\varphi)$ represents the appropriate thermodynamic potential and further validates our approach. For $n = 0.65$, $F(\varphi)$ attains minimum close to $\varphi = 180^\circ$, cf. Figs. 6(a) and 6(b). At intermediate densities ($n = 0.70$-0.75), Landau free energy is minimized by nontrivial values of φ [Figs. 6(b)–6(e)]. Finally, close to half-filling $n \gtrsim 0.8$, minimum shifts back toward $\varphi = 180^\circ$ [Figs. 6(f) and 6(g)]. This behavior reflects the domelike structures observed in Figs. 3(b) and 3(f). Remarkably though, the variation of $F(\varphi)$ in the range $\varphi \in [0, 360^\circ]$ does not exceed 60 μeV which is two orders of magnitude smaller than typical condensation energy for the t-J-U model in the high-T_c copper-oxide regime. We have thus established $\Delta F'_{\mathrm{SC}} \ll \Delta F_{\mathrm{SC}}$.

V. SUMMARY

We have studied the phase diagram of the t-J-U model on twisted square lattice, as a function of both hole doping and twist angle. The symmetry considerations allow us to establish a relationship between the solutions for complementary twist angles θ and $90^\circ - \theta$, which has been utilized to construct a complete superconducting phase diagram using a limited number of supercells. The latter mapping is exact in the thermodynamic limit, but controllable finite-size and boundary-condition effects are observed for finite lattices.

The phase diagram comprises both the gapless d-wave state and gapped TRS breaking topological $d + \mathrm{e}^{i\varphi}d$ phase. We have found that $d + \mathrm{e}^{i\varphi}d$ state occupies a nonconvex butterfly-shaped region in the density versus twist-angle phase diagram, resulting in reentrance of $d + \mathrm{e}^{i\varphi}d$ pairing as a function of twist angle θ close to half filling. One of the footprints of the SC state for nontrivial values of φ (i.e., $\varphi \neq 0^\circ, 180^\circ$) is the emergence of a gap in the quasiparticle energy spectrum, yet the gap magnitude is not related to SC phase angle φ in a straightforward manner. In particular, we have identified a multidome structure of energy gaps for certain values of layer twist angles.

The microscopically derived Landau free-energy functional exhibits a small variation as a function of the order-parameter relative phase, φ. In effect, the order parameter is susceptible to small perturbations. We have explicitly demonstrated that finite-size effects and boundary condition effects appear close to the TRS-breaking SC onset, where the free-energy landscape is particularly flat. This might rationalize reported difficulties with realization of the homogeneous $d + \mathrm{e}^{i\varphi}d$ state close to twist angle $\theta = 45^\circ$.

ACKNOWLEDGMENTS

M.F. and J.S. were partly supported by Grant Opus No. UMO-2021/41/B/ST3/04070 from Narodowe Centrum Nauki (NCN). B.R. was entirely supported by the project Opus No. UMO-2018/29/B/ST3/02646 from NCN.

APPENDIX A: STATISTICALLY-CONSISTENT GUTZWILLER APPROACH WITH ON-SITE SC PAIRING

The statistically consistent variational (Gutzwiller-type) approximation has been formulated and extensively analyzed elsewhere, see Refs. [1,28] and references therein. Here we summarize a specific variant of the latter that incorporates on-site SC pairing. This is needed to properly account for

the order-parameter symmetry in lattices with large unit cells, such as those emerging in twisted square-lattice systems.

The basic object within the SGA is variational energy functional

$$E_{\mathrm{var}} = \frac{\langle\Psi_{\mathrm{var}}|\hat{\mathcal{H}}|\Psi_{\mathrm{var}}\rangle}{\langle\Psi_{\mathrm{var}}|\Psi_{\mathrm{var}}\rangle}, \tag{A1}$$

where variational wave function is expressed as $|\Psi_{\mathrm{var}}\rangle \equiv \hat{\mathcal{P}}|\Psi_0\rangle$. Here $|\Psi_0\rangle$ denotes a Slater-determinant state and $\hat{\mathcal{P}}$ is the so-called *correlator* (an operator introducing correlations into the uncorrelated wave function $|\Psi_0\rangle$). We adopt the correlator in the form of a lattice product $\hat{\mathcal{P}} \equiv \prod_i \hat{\mathcal{P}}_i$, where

$$\hat{\mathcal{P}}_i \equiv \lambda_i^0|0\rangle_{ii}\langle 0| + \sum_{\sigma=\uparrow,\downarrow} \lambda_i^\sigma |\sigma\rangle_{ii}\langle\sigma| + \lambda_i^d|d\rangle_{ii}\langle d|. \tag{A2}$$

In Eq. (A2), the projection operators onto the local basis states ($|0\rangle_i$, $|\uparrow\rangle_i$, $|\downarrow\rangle_i$, and $|d\rangle_i \equiv |\uparrow\downarrow\rangle_i$) are multiplied by parameters λ_i^0, $\lambda_i^\uparrow$, $\lambda_i^\downarrow$, and λ_i^d. Both the λ parameters and uncorrelated state $|\Psi_0\rangle$ are variational objects that need to be determined by minimization of the functional E_{var}. In particular, $|\Psi_0\rangle$ encodes broken-symmetry states, including unconventional SC. Moreover, additional conditions on the λ parameters are needed to make the variational problem tractable, namely,

$$\langle\Psi_0|\hat{P}_i^2|\Psi_0\rangle = 1, \tag{A3}$$

$$\langle\Psi_0|\hat{P}_i\hat{n}_{i\uparrow}\hat{P}_i|\Psi_0\rangle = \langle\Psi_0|\hat{n}_{i\uparrow}|\Psi_0\rangle, \tag{A4}$$

$$\langle\Psi_0|\hat{P}_i\hat{n}_{i\downarrow}\hat{P}_i|\Psi_0\rangle = \langle\Psi_0|\hat{n}_{i\downarrow}|\Psi_0\rangle, \tag{A5}$$

where $\hat{n}_{i\sigma} \equiv \hat{a}_{i\sigma}^\dagger\hat{a}_{i\sigma}$ is the particle-number operator. In effect, the number of λ parameters is reduced from four to one per site; without loss of generality, one can select λ_i^d as the remaining one.

For specified microscopic Hamiltonian, $\hat{\mathcal{H}}$, the functional Eq. (A1) may be evaluated using Wick's theorem. Formally, variational energy becomes then a functional two-point expectation values of the form $\langle\Psi_0|\hat{a}_{i\sigma}^\dagger\hat{a}_{j\sigma'}|\Psi_0\rangle$, $\langle\Psi_0|\hat{a}_{i\sigma}^\dagger\hat{a}_{j\sigma'}^\dagger|\Psi_0\rangle$, $\langle\Psi_0|\hat{a}_{i\sigma}\hat{a}_{j\sigma'}|\Psi_0\rangle$, and correlator parameters. For brevity of notation, we denote the set of all two-point correlation function of this form as $\mathbf{P} = (P_1, P_2, \ldots)$ and dub them *lines*, whereas variational parameters are collectively marked as $\boldsymbol{\lambda} = (\lambda_1, \lambda_2, \ldots)$, where the indices enumerate all relevant degrees of freedom. Moreover, we introduce an analogous notation for the bilinear operators $\hat{\mathbf{P}} \equiv (\hat{P}_1, \hat{P}_2, \ldots)$ composed of the operator products $\hat{a}_{i\sigma}^\dagger\hat{a}_{j\sigma'}$, $\hat{a}_{i\sigma}^\dagger\hat{a}_{j\sigma'}^\dagger$, $\hat{a}_{i\sigma}\hat{a}_{j\sigma'}$ that are related to the corresponding lines as $\langle\Psi_0|\hat{P}_\gamma|\Psi_0\rangle \equiv P_\gamma$.

In effect, one can write $E_{\mathrm{var}} \equiv E_{\mathrm{var}}(\mathbf{P}, \boldsymbol{\lambda})$. Practical methods of evaluating the functional Eq. (A1) include variational Monte Carlo or specialized diagrammatic expansions in real space (diagrammatic expansion of the Guztwiller wave function) [29,30]. Here, we adopt the latter approach and retain only the leading-order diagrams (those that dominate in the large lattice-coordination-number limit). This results in the SGA [31].

We now proceed to formulation of our approach. Variational method amounts to minimization of the functional $E_{\mathrm{var}} \equiv E_{\mathrm{var}}(\mathbf{P}, \boldsymbol{\lambda})$ with respect to both $\mathbf{P}$ and $\boldsymbol{\lambda}$, with the additional constraints of fixed electron density and $P_\gamma \equiv \langle\Psi_0|\hat{P}_\gamma|\Psi_0\rangle$. The last condition ensures that the values of lines are compatible with some wave function that belongs to the underlying variational space. We employ a generalization of the plain variational method to finite temperature based on the free-energy functional

$$\mathcal{F}(\mathbf{P}, \boldsymbol{\lambda}, \boldsymbol{\rho}, \mu) = -\frac{1}{\beta}\ln \mathrm{Tr}\exp(-\beta\hat{\mathcal{H}}_{\mathrm{eff}}), \tag{A6}$$

where

$$\hat{\mathcal{H}}_{\mathrm{eff}}(\mathbf{P}, \boldsymbol{\lambda}, \boldsymbol{\rho}, \mu) \equiv E_{\mathrm{var}}(\mathbf{P}, \boldsymbol{\lambda}) + \sum_\gamma \rho_\gamma \cdot (\hat{P}_\gamma - P_\gamma) - \mu(\hat{N} - N_e) \tag{A7}$$

is the effective Hamiltonian describing the dynamics of correlated Fermi quasiparticles. In Eq. (A7), ρ_γ are Lagrange

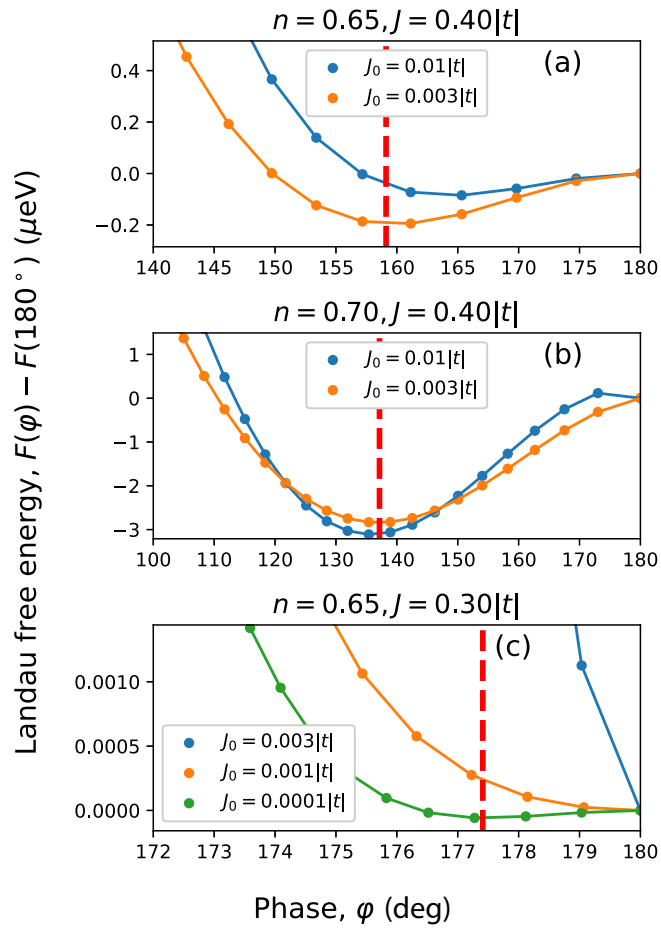

FIG. 7. Dependence of the Landau free-energy functional on the relative superconducting phase between layers, φ, for various selections of background current magnitude J_0 (cf. Appendix B for definition). The electronic density and exchange coupling are set to $n = 0.65, J = 0.4|t|$ (a), $n = 0.70, J = 0.4|t|$ (b), and $n = 0.65, J = 0.3|t|$ (c). The remaining parameters are the same as those used in the main text. Vertical dashed lines mark the self-consistently calculated SGA values for $J_0 \equiv 0$, representing true equilibrium solution. In the regime of large J and robust $d + e^{i\varphi}d$ SC, the equilibrium value is already reached for $J_0 = 0.003|t|$. However, for the smaller values of J and close to the topological phase boundary (c), the effective potential becomes practically flat (cf. the energy scale) and then much smaller values J_0 are required.

multipliers ensuring that the values of lines are compatible with thermodynamic expectation values, i.e.,

$$P_\gamma = \langle \hat{P}_\gamma \rangle \equiv \frac{\mathrm{Tr}\hat{P}_\gamma \mathrm{e}^{-\beta\hat{\mathcal{H}}_{\mathrm{eff}}}}{\mathrm{Tr}\mathrm{e}^{-\beta\hat{\mathcal{H}}_{\mathrm{eff}}}}. \tag{A8}$$

Moreover, the Lagrange multiplier μ is used to impose that the expectation value of the total particle number operator, $\langle \hat{N} \rangle$, is equal to target electron number N_e.

The system free energy F is determined as a stationary point of the free-energy functional over all fields that yield

$$\frac{\partial \mathcal{F}}{\partial P_\gamma} = \frac{\partial E_{\mathrm{var}}(\mathbf{P}, \boldsymbol{\lambda})}{\partial P_\gamma} - \rho_\gamma \equiv 0, \tag{A9}$$

$$\frac{\partial \mathcal{F}}{\partial \lambda_\gamma} = \frac{\partial E_{\mathrm{var}}(\mathbf{P}, \boldsymbol{\lambda})}{\partial \lambda_\gamma} \equiv 0, \tag{A10}$$

$$\frac{\partial \mathcal{F}}{\partial \rho_\gamma} = \langle \hat{P}_\gamma \rangle - P_\gamma \equiv 0, \tag{A11}$$

$$\frac{\partial \mathcal{F}}{\partial \mu} = \langle \hat{N} \rangle - N_e \equiv 0. \tag{A12}$$

In effect, we arrive at

$$F = \mathcal{F}(\tilde{\mathbf{P}}, \tilde{\boldsymbol{\lambda}}, \tilde{\boldsymbol{p}}, \tilde{\mu}), \tag{A13}$$

where $\tilde{\mathbf{P}}$, $\tilde{\boldsymbol{\lambda}}$, $\tilde{\boldsymbol{p}}$, and $\tilde{\mu}$ denote equilibrium (saddle-point) values of the lines, correlator parameters, and Lagrange multipliers. Equations (A9)–(A12) are solved by self-consistent iteration. Due to substantial computational cost involved for large supercells and slow asymptotic convergence for the $d + \mathrm{e}^{i\varphi} d$ SC state in the strong-coupling limit, we have modified the usual self-consistent loop by employing Anderson acceleration scheme [32].

Equivalence of the thermal variational problem based on Eq. (A6) and plain zero-temperature calculation may be established by recasting Eq. (A13) in a different form

$$F = E_{\mathrm{var}}(\tilde{\mathbf{P}}, \tilde{\boldsymbol{\lambda}}) - TS, \tag{A14}$$

where the entropy reads

$$S = -k_B \sum_\alpha [\tilde{n}_\alpha \ln \tilde{n}_\alpha + (1 - \tilde{n}_\alpha) \ln(1 - \tilde{n}_\alpha)]. \tag{A15}$$

In Eq. (A15), the summation index α enumerates eigenstates of the effective Hamiltonian, $\hat{\mathcal{H}}_{\mathrm{eff}}$, and $\tilde{n}_\alpha$ denotes their equilibrium occupation numbers. By taking $T \to 0$, the problem is thus reduced to optimization of the plain energy functional, and the thermal expectation values reduce to ground-state averages.

APPENDIX B: LANDAU FREE-ENERGY FUNCTIONAL AND FINITE-SIZE EFFECTS

The free energy, F, is a function of temperature and microscopic model parameters (including hopping integrals, Coulomb repulsion, and antiferromagnetic exchange), but does not depend on the superconducting order parameter, cf. Eq. (A13). To analyze the evolution of the energetic landscape as a function of twist angle, one thus needs to carry out the Legendre transform of F and evaluate the *effective potential* with respect to auxiliary currents coupled to the $d + \mathrm{e}^{i\varphi} d$ order parameter. We follow the condensed-matter convention, and hereafter refer to it as the Landau free-energy functional.

First, we define the extended Hamiltonian

$$\hat{\mathcal{H}}'(\mathbf{J}) \equiv \hat{\mathcal{H}} - \mathbf{J}^\dagger \hat{\boldsymbol{\Delta}} - \hat{\boldsymbol{\Delta}}^\dagger \mathbf{J}, \tag{B1}$$

where $\mathbf{J} \equiv (J^{(A)}, J^{(B)})^T$ is a two-component complex external pairing field and $\hat{\boldsymbol{\Delta}} \equiv (\hat{\Delta}^{(A)}, \hat{\Delta}^{(B)})^T$ is the $d + \mathrm{e}^{i\varphi} d$ SC operator for twisted bilayer [cf. Eqs. (5)-(6)]. The superscript T indicates transposition. For compactness, we write $\hat{\mathcal{H}}(\mathbf{J})$ rather than $\hat{\mathcal{H}}(\mathbf{J}, \mathbf{J}^\dagger)$, keeping in mind that $\mathbf{J}$ is complex and $\hat{\mathcal{H}}$ depends both on $\mathbf{J}$ and $\mathbf{J}^\dagger$, so it remains manifestly Hermitian, cf. Eq. (B1). The same shorthand notation is employed for all functionals introduced below.

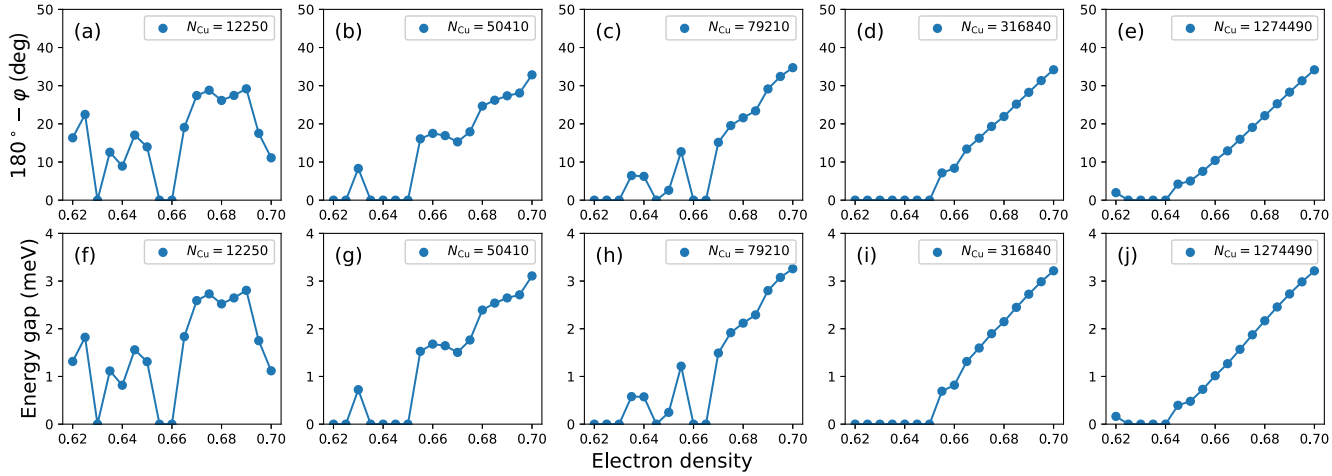

FIG. 8. Illustration of the finite-size effects on topological superconducting state in twisted cuprates for twist angle $\theta = 53.13^\circ$ and $J = 0.3|t|$. The remaining model parameters are listed in Sec. II of the main text. (a)–(e) Doping dependence of the relative order parameter phase φ for various total system sizes spanning two orders of magnitude (employed number of copper sited, N_{Cu}, is detailed inside the panels). (f)–(j) Corresponding values of energy gap. Starting from $N_{\mathrm{Cu}} \sim 80\,000$ superconductivity with gaps >1 meV stabilizes and reflects thermodynamic-limit behavior, but small finite-size effects are still visible in the sub-meV energy range.

One can now repeat the procedure described in Appendix A for the extended Hamiltonian $\hat{\mathcal{H}}'(\mathbf{J})$ and evaluate the corresponding free energy $F'(\mathbf{J})$ as a function of pairing field, $\mathbf{J}$. The expectation value of the order parameter depends on $\mathbf{J}$ and may be expressed as

$$\mathbf{\Delta} \equiv -\frac{\partial F'(\mathbf{J})}{\partial \mathbf{J}^\dagger}, \tag{B2}$$

$$\mathbf{\Delta}^\dagger \equiv -\frac{\partial F'(\mathbf{J})}{\partial \mathbf{J}}, \tag{B3}$$

The Landau free energy is defined as

$$F(\mathbf{\Delta}) \equiv F'[\mathbf{J}(\mathbf{\Delta})] + \mathbf{J}^\dagger(\mathbf{\Delta})\mathbf{\Delta} + \mathbf{\Delta}^\dagger\mathbf{J}(\mathbf{\Delta}), \tag{B4}$$

where the dependence of background currents on the order parameter, $\mathbf{J}(\mathbf{\Delta})$ and $\mathbf{J}^\dagger(\mathbf{\Delta})$, is obtained by inverting Eqs. (B2) and (B3).

As is apparent from Eq. (B4), the Landau free energy is a functional a complex two-component field, $\mathbf{\Delta}$, which syields four real degrees of freedom. Since evaluation of $F(\mathbf{\Delta})$ is a numerically expensive task, we now propose a way to reduce the number of free parameters from four to one. First, it should be noted that $F(\mathbf{\Delta})$ is invariant with respect to a global gauge transformation $\mathbf{\Delta} \to \exp(i\phi)\mathbf{\Delta}$. In turn, the global phase angle ϕ might be outright eliminated so only three nontrivial degrees of freedom in the order-parameter $\mathbf{\Delta}$ remain. Without loss of generality, one can select the layer SC amplitudes $|\Delta^{(A)}|$ and $|\Delta^{(B)}|$, and relative phase, $\varphi = \arctan(\Delta^{(B)}/\Delta^{(A)})$. The final simplification is based on the circumstance that there the energy scales related to the SC transition and variation of relative phase φ are well separated and may be analyzed independently (cf. discussion in Sec. IV C). We thus fix the pairing amplitudes $|\Delta^{(A)}|$ and $|\Delta^{(B)}|$ by imposing two constraints on the amplitudes of background currents in Eqs. (B2) and (B3), namely, $|J^{(A)}| = J_0$ and $|J^{(B)}| = J_0$ with J_0 being a small positive number. Strictly speaking, the SC amplitudes attain their equilibrium values for $J_0 \to 0$ or, equivalently, $\mathbf{J} = \mathbf{0}$. Indeed, by combining Eqs. (A9), (A10), and (B4), one can verify that

$$\frac{\partial F(\mathbf{\Delta})}{\partial \mathbf{\Delta}^\dagger} = \mathbf{J}, \tag{B5}$$

so the necessary condition for the Landau free-energy minimum $\frac{\partial F(\mathbf{\Delta})}{\partial \mathbf{\Delta}^\dagger} = \mathbf{0}$ is equivalent to vanishing of the background currents, $\mathbf{J}$. However, keeping a small finite J_0 improves performance and ensures stability of solutions in a broad range of φ, so we typically retain a nonzero value of J_0 in our calculations while evaluating $F(\mathbf{\Delta})$. Based on numerical experiments, we have found that $J_0 = 0.003|t|$ is sufficiently small not to alter the equilibrium value of φ for most microscopic parameter configurations considered, and allows us to efficiently map the free-energy landscape as a function of SC relative phase angle.

In Fig. 7, we analyze the scaling of $F(\varphi)$ as a function of J_0 for selected values of electron density and antiferromagnetic exchange coupling, J, detailed above the panels. All other parameters are listed in Sec. II of the main text. The vertical dashed lines show the values of relative SC phase φ, obtained for self-consistent iteration with $J_0 = 0$ and thus reflecting the equilibrium state. As is apparent from Fig. 7(a) for $J_0 = 0.01|t|$, the functional $F(\varphi)$ attains its minimum at

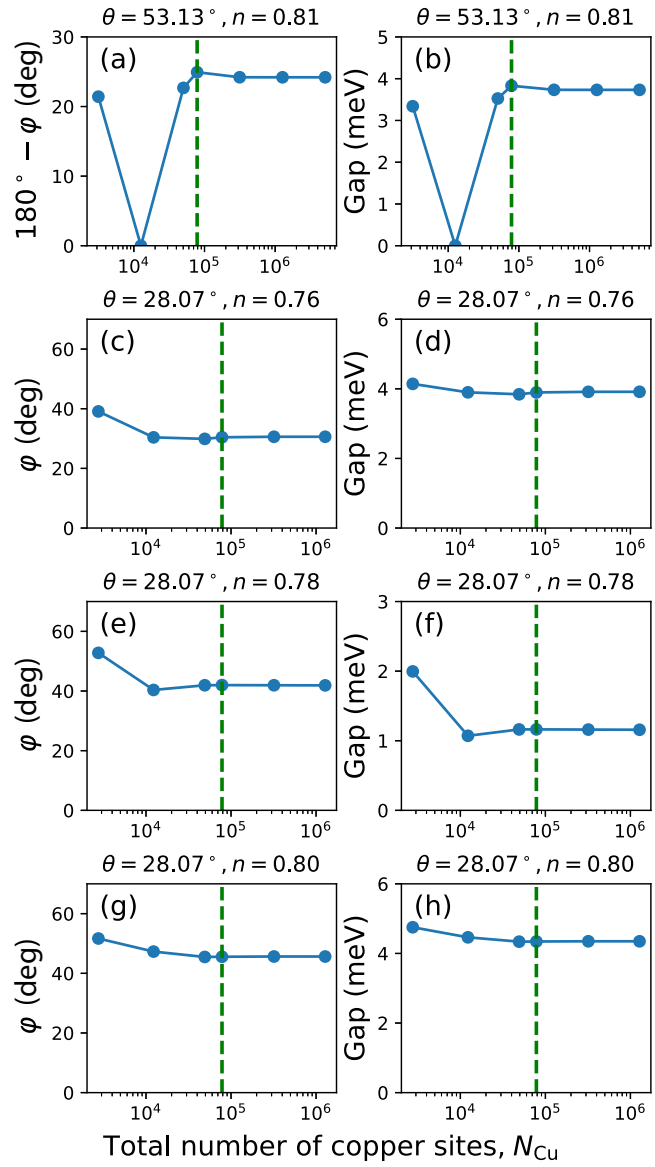

FIG. 9. Finite-size scaling of topological superconducting domes for antiferromagnetic exchange $J = 0.3|t|$; the remaining model parameters are the same as those listed in Sec. II of the main text. (a), (b) Dependence of the order-parameter phase angle φ and energy on the total number of copper atoms, N_{Cu}, for the twist angle $\theta = 53.13^\circ$ and electron concentration $n = 0.81$. Dashed vertical lines mark the system size (≈80 000 Cu sites) used to generate the phase diagrams presented in the main text. (c)–(h) An analogous scaling carried out for twist angle $\theta = 28.07^\circ$ and doping levels $n = 0.76, 0.78$, and 0.80 [encompassing the uncommon double superconducting dome seen in Fig. 3(g) for this value of θ]. The finite-size scaling proves that the results displayed in Fig. 3 accurately represent the thermodynamic limit situation. The twin-dome behavior is thus not an artifact, but reflects the physics of bulk twisted bilayer system [cf. Fig. 3(g) and panels (d), (f), and (g) of the present figure].

nontrivial angle $\varphi \approx 165^\circ$ (blue curve) that differs from true equilibrium value $\varphi \approx 159^\circ$ (vertical red line). By reducing J_0 to $0.003|t|$, the minimum of the Landau free energy shifts to its equilibrium position. This shows that $J_0 \lesssim 0.003|t|$

already provides a reliable representation of the $J_0 \to 0$ limit situation. Parenthetically, the scaling presented in Fig. 7(a) corresponds to the lower boundary, the topological $d + e^{i\varphi}d$ state for $\theta = 53.13^\circ$ and $J = 0.4|t|$ [cf. the dome for complementary angle 36.87° in the phase diagram of Figs. 3(b) and 3(c)]. In Fig. 7(b), we show an analogous scaling deep inside the dome formed by the topological SC state. In this case, we conclude that, already for $J_0 = 0.01|t|$, the exact position of the Landau free-energy minimum (i.e., that obtained by self-consistent iteration for $J_0 = 0$) is accurately determined, and the Landau free-energy minimum is deeper than the corresponding one close to the onset of the gapped state [Fig. 7(a)]. We also note that the exact value of the relative SC phase φ is highly sensitive to even a small change of J_0 on the boundary of the topological state and becomes fairly robust with the increase of the energy gap. In Fig. 7(c), we demonstrate an extreme case of such a fragile topological state for a fine-tuned set of parameters close to the $d + e^{i\varphi}d$ dome boundary ($n = 0.65|t|$ and $J = 0.3|t|$). Here J_0 as low as $0.0001|t|$ is needed to match the self-consistently obtained relative phase. The situation presented in Fig. 7(c) is not common and occurs only in regime of very weak topological SC. The free energy landscape is then particularly flat (variation of $F(\varphi)$ within the range of neV), contrary to typical cases displayed in Figs. 7(a) and 7(b), where $F(\varphi)$ varies at the μeV scale.

The above consideration allow us to draw a few general conclusions. First, due to the flatness of the free-energy landscape, topological SC is expected to by highly sensitive to boundary conditions and finite-size effects at the topological state boundary, even for relatively large lattices. This is clearly seen in Figs. 3(b), 3(c), 3(f) and 3(g), where the equilibrium phase and energy gap becomes noisy at the SC dome corners. However, deep within the $d + e^{i\varphi}d$ state, no noise is observed. Below we carry out a systematic finite-size scaling to further explore those effects. Second, reliable evaluation of equilibrium relative phase φ requires high numerical accuracy. In the present paper, we have set the target absolute precision for the dimensionless two-point correlation functions to 10^{-10} to achieve this goal. With the number of integral equations to be solved self-consistently, exceeding 10^3 for largest considered supercells ($\theta = 43.6^\circ$), this makes the problem computationally challenging. In particular, for certain densities and $\theta = 43.6^\circ$ in the phase diagrams of Figs. 3(a) and 3(e), we were unable to obtain the SGA solution with the target accuracy of 10^{-10} (missing points). This happens, in particular, at small doping, where the correlation effects increase as the metal to insulator transition is approached.

Now we address in detail the finite-size effects by focusing on layer twist angle $\theta = 53.13^\circ$ and $J = 0.3|t|$. The remaining model parameters are presented in Sec. II of the main text. Figure 8 shows the electron-density-dependence of the relative SC phase φ [Figs. 8(a)–8(e)] and energy gap in the quasiparticle spectrum [Figs. 8(f)–8(j)], for various lattice sizes increasing from left to right. The exact number of copper sites in the system, N_{Cu}, is listed inside the panels and spans two orders of magnitude (from 12 250 to 1 274 490). The electron densities cover the lower end of the topological $d + e^{i\varphi}d$ state, where finite-size effects are expected to be particularly relevant, cf. the discussion in Appendix. B. As follows from Fig. 8, both φ and the energy gap fluctuate substantially as a function of electron concentration for the smallest lattice sizes considered. The underlying reason is flatness of the Landau free-energy functional, so even fairly weak finite-size effects may affect the equilibrium value of relative SC phase. Above $N_{\mathrm{Cu}} \sim 80\,000$, both φ and gaps start to stabilize, also in the sub-meV range. We thus consider N_{Cu} as a threshold value that may be regarded as a representation of the thermodynamic-limit situation. The results reported in the main text have been obtained with lattices containing $N_{\mathrm{Cu}} \approx 80\,000$ sites.

To further investigate saturation of the topological SC characteristics with increasing lattice size, in Fig. 9 we carry out finite size-scaling for $J = 0.3|t|$, and twist angles $\theta = 53.13^\circ$ and $\theta = 28.07^\circ$, across the $d + e^{i\varphi}d$ SC dome. The relevant parameters are listed above the panels, and those unspecified are given in Sec. II of the main text. Dashed vertical lines mark the lattice sizes $N_{\mathrm{Cu}} \approx 80\,000$, used to generate the phase diagram of Fig. 3. The finite-size scaled quantities exhibit saturation above $N_{\mathrm{Cu}} \approx 80\,000$. We also point out that the results displayed in Figs. 9(d), 9(f) and 9(h) provide robust evidence for the existence of the two-dome structure [cf. green curve in Fig. 3(g)]. Indeed, the saturated value of the energy gap initially decreases from ≈4 meV to ≈1 meV as electron density changes from $n = 0.76$ to $n = 0.78$, and then increases again to ≈4 meV at $n = 0.80$.

[1] J. Spałek, M. Fidrysiak, M. Zegrodnik, and A. Biborski, Superconductivity in high-T_c and related strongly correlated systems from variational perspective: Beyond mean field theory, Phys. Rep. **959**, 1 (2022).

[2] Y. Cao, V. Fatemi, S. Fang, K. Watanabe, T. Taniguchi, E. Kaxiras, and P. Jarillo-Herrero, Unconventional superconductivity in magic-angle graphene superlattices, Nature (London) **556**, 43 (2018).

[3] Y. Cao, V. Fatemi, A. Demir, S. Fang, S. L. Tomarken, J. Y. Luo, J. D. Sanchez-Yamagishi, K. Watanabe, T. Taniguchi, E. Kaxiras, R. C. Ashoori, and P. Jarillo-Herrero, Correlated insulator behaviour at half-filling in magic-angle graphene superlattices, Nature (London) **556**, 80 (2018).

[4] L. Wang, E.-M. Shih, A. Ghiotto, L. Xian, D. A. Rhodes, C. Tan, M. Claassen, D. M. Kennes, Y. Bai, B. Kim, K. Watanabe, T. Taniguchi, X. Zhu, J. Hone, A. Rubio, A. N. Pasupathy, and C. R. Dean, Correlated electronic phases in twisted bilayer transition metal dichalcogenides, Nat. Mater. **19**, 861 (2020).

[5] S. Y. Frank Zhao, N. Poccia, M. G. Panetta, C. Yu, J. W. Johnson, H. Yoo, R. Zhong, G. D. Gu, K. Watanabe, T. Taniguchi, S. V. Postolova, V. M. Vinokur, and P. Kim, Sign-reversing Hall effect in atomically thin high-temperature $Bi_{2.1}Sr_{1.9}CaCu_{2.0}O_{8+\delta}$ superconductors, Phys. Rev. Lett. **122**, 247001 (2019).

[6] M. Liao, Y. Zhu, J. Zhang, R. Zhong, J. Schneeloch, G. Gu, K. Jiang, D. Zhang, X. Ma, and Q.-K. Xue,

Superconductor-insulator transitions in exfoliated $Bi_2Sr_2CaCu_2O_{8+x}$ flakes, Nano Lett. **18**, 5660 (2018).

[7] Y. Yu, L. Ma, P. Cai, R. Zhong, C. Ye, J. Shen, G. D. Gu, X. H. Chen, and Y. Zhang, High-temperature superconductivity in monolayer $Bi_2Sr_2CaCu_2O_{8+x}$, Nature (London) **575**, 156 (2019).

[8] O. Can, T. Tummuru, R. P. Day, I. Elfimov, A. Damascelli, and M. Franz, High-temperature topological superconductivity in twisted double-layer copper oxides, Nat. Phys. **17**, 519 (2021).

[9] Z. Yang, S. Qin, Q. Zhang, C. Fang, and J. Hu, $\pi/2$-Josephson junction as a topological superconductor, Phys. Rev. B **98**, 104515 (2018).

[10] X. Lu and D. Sénéchal, Doping phase diagram of a Hubbard model for twisted bilayer cuprates, Phys. Rev. B **105**, 245127 (2022).

[11] X.-Y. Song, Y.-H. Zhang, and A. Vishwanath, Doping a moiré Mott insulator: A t-J model study of twisted cuprates, Phys. Rev. B **105**, L201102 (2022).

[12] Y. Zhu, M. Liao, Q. Zhang, H.-Y. Xie, F. Meng, Y. Liu, Z. Bai, S. Ji, J. Zhang, K. Jiang, R. Zhong, J. Schneeloch, G. Gu, L. Gu, X. Ma, D. Zhang, and Q.-K. Xue, Presence of s-wave pairing in Josephson junctions made of twisted ultrathin $Bi_2Sr_2CaCu_2O_{8+x}$ flakes, Phys. Rev. X **11**, 031011 (2021).

[13] J. Lee, W. Lee, Y. Choi, Y. Choi, J. Park, S. H. Jang, G. Gu, S. Choi, G. Y. Cho, G. Lee, and H. Lee, Twisted van der Waals Josephson junction based on a high-T_c superconductor, Nano Lett. **21**, 10469 (2021).

[14] M. Martini, Y. Lee, T. Confalone, S. Shokri, C. N. Saggau, D. Wolf, G. Gu, K. Watanabe, T. Taniguchi, D. Montemurro, V. M. Vinokur, K. Nielsch, and N. Poccia, Twisted cuprate van der Waals heterostructures with controlled Josephson coupling, Mater. Today **67**, 106 (2023).

[15] S. Y. F. Zhao, N. Poccia, X. Cui, P. A. Volkov, H. Yoo, R. Engelke, Y. Ronen, R. Zhong, G. Gu, S. Plugge, T. Tummuru, M. Franz, J. H. Pixley, and P. Kim, Emergent interfacial superconductivity between twisted cuprate superconductors, arXiv:2108.13455.

[16] H. Wang, Y. Zhu, Z. Bai, Z. Wang, S. Hu, H.-Y. Xie, X. Hu, J. Cui, M. Huang, J. Chen, Y. Ding, L. Zhao, X. Li, Q. Zhang, L. Gu, X. J. Zhou, J. Zhu, D. Zhang, and Q.-K. Xue, Prominent Josephson tunneling between twisted single copper oxide planes of $Bi_2Sr_{2-x}LaxCuO_{6+y}$, Nat. Commun. **14**, 5201 (2023).

[17] J. Spałek, M. Zegrodnik, and J. Kaczmarczyk, Universal properties of high-temperature superconductors from real-space pairing: t-J-U model and its quantitative comparison with experiment, Phys. Rev. B **95**, 024506 (2017).

[18] M. Fidrysiak, M. Zegrodnik, and J. Spałek, Realistic estimates of superconducting properties for the cuprates: Reciprocal-space diagrammatic expansion combined with variational approach, J. Phys.: Condens. Matter **30**, 475602 (2018).

[19] G. Deutscher, A. F. Santander-Syro, and N. Bontemps, Kinetic energy change with doping upon superfluid condensation in high-temperature superconductors, Phys. Rev. B **72**, 092504 (2005).

[20] J. Levallois, M. K. Tran, D. Pouliot, C. N. Presura, L. H. Greene, J. N. Eckstein, J. Uccelli, E. Giannini, G. D. Gu, A. J. Leggett, and D. van der Marel, Temperature-dependent ellipsometry measurements of partial Coulomb energy in superconducting cuprates, Phys. Rev. X **6**, 031027 (2016).

[21] K. A. Chao, J. Spałek, and A. M. Oleś, Kinetic exchange interaction in a narrow S-band, J. Phys. C **10**, L271 (1977).

[22] M. Zegrodnik and J. Spałek, Effect of interlayer processes on the superconducting state within the t-J-U model: Full Gutzwiller wave-function solution and relation to experiment, Phys. Rev. B **95**, 024507 (2017).

[23] R. S. Markiewicz, S. Sahrakorpi, M. Lindroos, H. Lin, and A. Bansil, One-band tight-binding model parametrization of the high-T_c cuprates including the effect of k_z dispersion, Phys. Rev. B **72**, 054519 (2005).

[24] T. Fukui, Y. Hatsugai, and H. Suzuki, Chern numbers in discretized Brillouin zone: Efficient method of computing (spin) Hall conductances, J. Phys. Soc. Jpn. **74**, 1674 (2005).

[25] R. B. Laughlin, Gossamer superconductivity, Philos. Mag. **86**, 1165 (2006).

[26] J. W. Loram, J. L. Luo, J. R. Cooper, W. Y. Liang, and J. L. Tallon, The condensation energy and pseudogap energy scale of Bi:2212 from the electronic specific heat, Physica C **341-348**, 831 (2000).

[27] T. Matsuzaki, N. Momono, M. Oda, and M. Ido, Electronic specific heat of $La_{2-x}Sr_xCuO_4$: pseudogap formation and reduction of the superconducting condensation energy, J. Phys. Soc. Jpn. **73**, 2232 (2004).

[28] J. Jędrak, J. Kaczmarczyk, and J. Spałek, Statistically-consistent Gutzwiller approach and its equivalence with the mean-field slave-boson method for correlated systems, arXiv:1008.0021.

[29] J. Bünemann, T. Schickling, and F. Gebhard, Variational study of Fermi surface deformations in Hubbard models, Europhys. Lett. **98**, 27006 (2012).

[30] J. Kaczmarczyk, J. Bünemann, and J. Spałek, High-temperature superconductivity in the two-dimensional t-J model: Gutzwiller wavefunction solution, New J. Phys. **16**, 073018 (2014).

[31] J. Jędrak and J. Spałek, Renormalized mean-field t-J model of high-T_c superconductivity: Comparison to experiment, Phys. Rev. B **83**, 104512 (2011).

[32] N. C. Henderson and R. Varadhan, Damped anderson acceleration with restarts and monotonicity control for accelerating EM and EM-like algorithms, J. Comput. Graph. Stat. **28**, 834 (2019).